

Article

Processing and Characterization of High-Density Fe-Silicide/Si Core–Shell Quantum Dots for Light Emission

Katsunori Makihara ^{1,2,*} , Yuji Yamamoto ^{1,2} , Markus Andreas Schubert ² , Andreas Mai ² 
and Seiichi Miyazaki ³

¹ Graduate School of Engineering, Nagoya University, Nagoya 464-8601, Japan; yamamoto@ihp-microelectronics.com

² IHP-Leibniz-Institut für Innovative Mikroelektronik, 15236 Frankfurt, Germany; schuberta@ihp-microelectronics.com (M.A.S.); mai@ihp-microelectronics.com (A.M.)

³ Hiroshima University, Higashihiroshima 739-0046, Japan; semiya1@hiroshima-u.ac.jp

* Correspondence: makihara.katsunori.n6@f.mail.nagoya-u.ac.jp; Tel.: +81-52-789-2727

Abstract: Si-based photonics has garnered considerable attention as a future device for complementary metal–oxide–semiconductor (CMOS) computing. However, few studies have investigated Si-based light sources highly compatible with Si ultra large-scale integration processing. In this study, we observed stable light emission at room temperature from superatom-like β -FeSi₂-core/Si-shell quantum dots (QDs). The β -FeSi₂-core/Si-shell QDs, with an areal density as high as $\sim 10^{11}$ cm⁻² were fabricated by self-aligned silicide process of Fe-silicide capped Si-QDs on ~ 3.0 nm SiO₂/n-Si (100) substrates, followed by SiH₄ exposure at 400 °C. From the room temperature photoluminescence characteristics, β -FeSi₂ core/Si-shell QDs can be regarded as active elements in optical applications because they offer the advantages of photonic signal processing capabilities and can be combined with electronic logic control and data storage.

Keywords: Fe-silicide; core/shell structure; CVD



Academic Editor: Chunxiang Xu

Received: 14 April 2025

Revised: 9 May 2025

Accepted: 13 May 2025

Published: 14 May 2025

Citation: Makihara, K.; Yamamoto, Y.; Schubert, M.A.; Mai, A.; Miyazaki, S. Processing and Characterization of High-Density Fe-Silicide/Si Core–Shell Quantum Dots for Light Emission. *Nanomaterials* **2025**, *15*, 733. <https://doi.org/10.3390/nano15100733>

Copyright: © 2025 by the authors. Licensee MDPI, Basel, Switzerland. This article is an open access article distributed under the terms and conditions of the Creative Commons Attribution (CC BY) license (<https://creativecommons.org/licenses/by/4.0/>).

1. Introduction

The monolithic integration of Si-based photonics with electronic processes on a single chip is considered a key advancement for beyond-complementary metal–oxide–semiconductor (CMOS) computing [1–9]. Photonic components utilize photons allowing for the highest level of precision and highly efficient data processing and transmission, resulting in faster and more energy-efficient devices. However, from an application point of view, Si-based photonics necessitate Si-based light sources that are highly compatible with Si-ultra-large-scale integration (Si-ULSI) processing [10–34]. Most importantly, despite the excellent optical properties of Si-based light emitters due to their high refractive index and the high-quality Si/SiO₂ interface, which means low defect density, they suffer from the inherent indirect band gap of Si, resulting in long carrier lifetimes and inefficient light emission. Therefore, integration of Si-based photonic processing with electrical processing on a single chip remains a significant challenge. In this study, we report on light emission from Si quantum dots (QDs) with a β -FeSi₂ core referred to as superatom-like QDs. β -FeSi₂ is a semiconductor phase with an indirect bandgap of ~ 0.7 eV, close to the direct bandgap value (~ 0.85 eV) at room temperature and shows light emission in the near-infrared region [35–43]. Therefore, to achieve good thermal stability and light emission characteristics, β -FeSi₂ is one of the promising candidates.

Si-based QDs have garnered significant attention due to their potential application as active elements in group IV photonics, driven by their light emission properties attributed to the carrier confinement effect. Previously, we reported the self-assembly of Si-QDs with an areal density as high as $\sim 10^{11}$ cm $^{-2}$ on ultrathin SiO $_2$ by controlling the early stages of thermal decomposition of SiH $_4$, showcasing their light emission properties [44–46]. More recently, we also detailed the formation of the β -FeSi $_2$ nanodots (NDs) through the exposure of an ultrathin Fe layer to a remote H $_2$ plasma (H $_2$ -RP) followed by SiH $_4$ exposure, and characterized their photoluminescence (PL) properties [47–49]. In this work, we successfully formed high-density Si-shell/ β -FeSi $_2$ -core QDs, akin to superatoms, with a uniform size distribution by controlling self-aligned silicidation of the Si-QDs and subsequent selective Si growth at low temperature to minimize metal diffusion. Furthermore, we discovered that light emission with a narrow wavelength range at room temperature from the Si-QD with a β -FeSi $_2$ core was due to radiative recombination between the electron-quantized state in the core and the hole-quantized state in the shell, indicating that the Si-QD with a β -FeSi $_2$ -core is a promising light-emitting material for Si-based photonics.

2. Materials and Methods

To systematically investigate the silicide process and selective Si growth, Si on insulator (SOI) substrates was used in this study, with a SiO $_2$ thickness of ~ 145 nm. Figure 1a–d schematically illustrates the concept of the experiment. Initially, the Si layer on the SiO $_2$ was thinned to ~ 10 nm by alternately controlling the thermal oxidation and wet etching using a diluted HF solution. Subsequently, ~ 1.0 nm thick Fe films were deposited via electron-beam evaporation. Film thickness in these experiments was evaluated by spectroscopic ellipsometry. The Fe film was then immediately removed using a HCl solution. Following this, the sample was exposed to SiH $_4$ at 400 °C, with total gas pressure and exposure duration of 100 Pa and 1800 s, respectively.

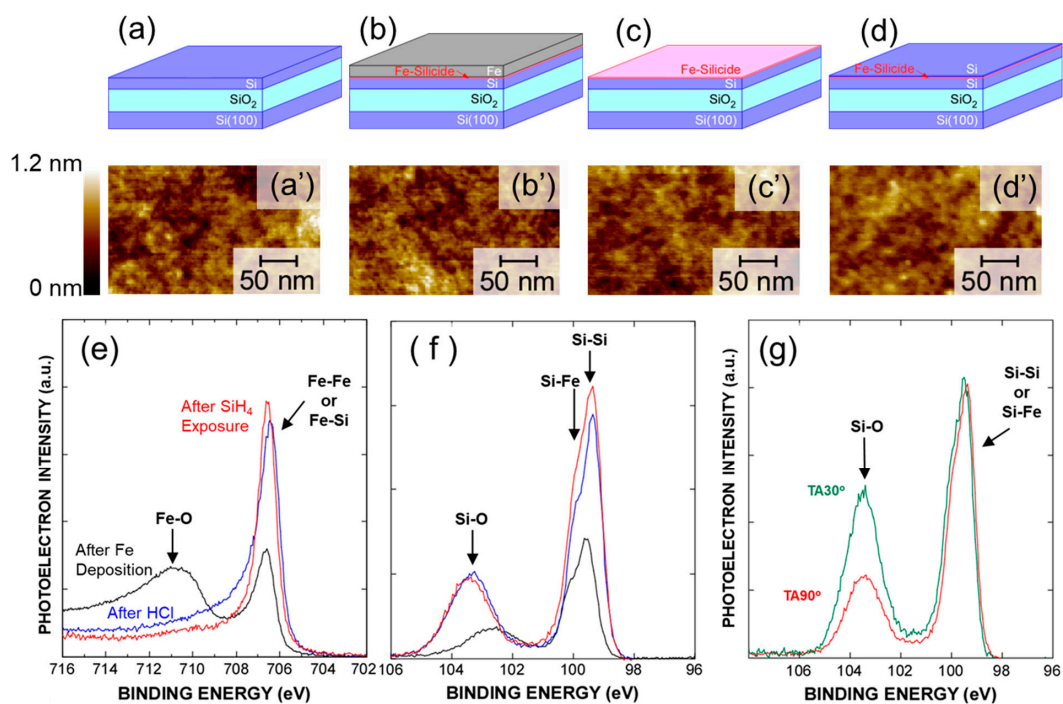


Figure 1. (a–d) Schematic illustration at each process step, and corresponding (a'–d') typical AFM images of (a,a') SOI surface, (b,b') taken after Fe film deposition, (c,c') after HCl treatment, and (d,d') after subsequent SiH $_4$ exposure. (e) Fe2p, and (f,g) Si2p core-line spectra of Fe/SOI substrate before and after HCl treatment, and after SiH $_4$ exposure taken at photoelectron take-off angle of (e,f) 90° and (g) 30°.

3. Formation of Ultrathin Si/Fe-Silicide/Si Structures

Figure 1a'–d' shows atomic force microscopy (AFM) images taken after each process step. The root mean square (RMS) roughness of the SOI substrate surface evaluated from the AFM image was as low as ~ 0.15 nm, which is almost the same as that before the thinning of the Si layer. AFM images of the surface taken after Fe film deposition and subsequent removal of the Fe film confirmed that the RMS roughness remained the same as before Fe deposition, as shown in Figure 1b',c'. Furthermore, no significant change in the RMS roughness was observed after SiH₄ exposure, indicating an extremely flat surface at each process step. To evaluate the chemical bonding features of the surface, we analyzed Si 2p_{3/2} and Fe 2p_{3/2} spectra of the Fe/SOI structure before and after HF etching and subsequent SiH₄ exposure, as shown in Figure 1e and Figure 1f, respectively, measured by X-ray photoelectron spectroscopy (XPS) using monochromatized Al-K α radiation ($h\nu = 1486.6$ eV), with the binding energy of each spectrum normalized by the C 1s signal. However, an Fe oxide component in the Fe 2p spectrum after Fe deposition was observed due to air exposure during XPS measurements, which was hardly observed prior to HCl treatment. This result indicates that the unreacted Fe and Fe oxide were completely etched by the HCl treatment. Interestingly, the signal intensity originating from the Si–Si and/or Si–Fe component increased and slightly shifted towards the lower binding energy side after HCl treatment compared to that after Fe film deposition, suggesting that the silicidation reaction of the Si layer surface was induced just after Fe film deposition, despite the absence of heating. In other words, the silicidation reaction proceeds through the deposition of the Fe film onto an atomically flat Si surface, followed by its removal using HCl, without any post-deposition annealing. It is well established that, in silicide systems, the resulting crystal phase is determined by the composition ratio [50]. Therefore, in our process, the silicidation is self-limited due to Fe-supply limited kinetics, which leads to the formation of an abrupt interface. Following SiH₄ exposure, the Si–Si and/or Si–Fe signal intensities slightly increased while the oxidation of Fe–silicide remains suppressed. Therefore, to evaluate the impact of changes in the chemical bonding features on the sample surface after the SiH₄ exposure, the Si 2p_{3/2} spectra were also measured at a photoelectron take-off angle of 30°, as indicated in Figure 1g. Angle-resolved analysis of Si2p after SiH₄ exposure showed a significant increase in the Si oxide component in the surface-sensitive measurement at a photoelectron take-off angle of 30°. These results might be attributed to the SiH₄ decomposition on the Fe–silicide layer surface even at 400 °C, followed by the growth of a Si layer on the silicide layer surface. In the case of Ni silicide, it is known that the silicidation reaction proceeds at low temperature, as the Ni-adamantane structure serves as a precursor for the formation of NiSi₂ [51]. Whether a similar mechanism is operative in the Fe silicide system remains an open question, which we aim to address in future studies.

The formation of the ultrathin Fe–silicide layer and Si growth on the silicide layer was confirmed through cross-sectional transmission electron microscopy (TEM) energy-dispersive X-ray spectroscopy (EDX) mapping images, as illustrated in Figure 2a–d. The TEM lamella is prepared by mechanical grinding and polishing followed by Ar ion milling. Despite the Fe film being deposited at room temperature and subsequently etched by HCl, the formation of an ultrathin Fe layer was observed. In contrast, Si signals were detected throughout the sample, irrespective of the film thickness direction. It was confirmed that the top surface of the sample was oxidized, and these results were consistent with those obtained from the XPS analysis. Furthermore, the growth of Si on the Fe surface was confirmed by analyzing the atomic concentration of each element in the film thickness direction, as evaluated from the cross-sectional profile as shown in Figure 2d, indicating the formation of a sandwich structure in which the Fe–silicide layer was sandwiched between

the Si layers. It is noteworthy that the atomic concentration ratio of Fe to Si was close to 1:2, suggesting the formation of the FeSi₂ phase.

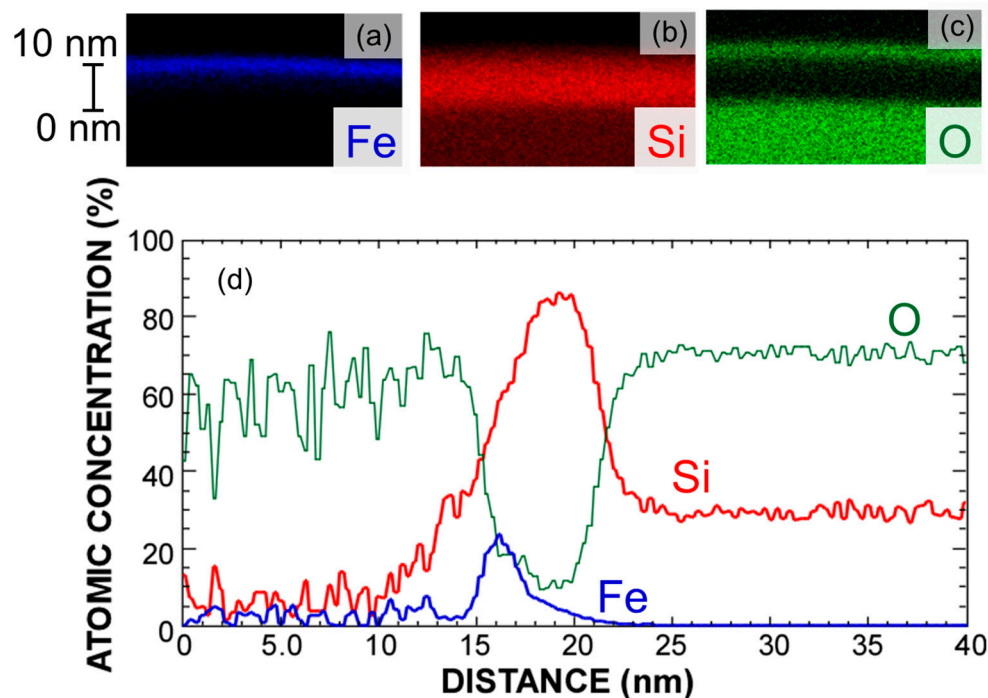


Figure 2. (a–c) Cross-sectional EDX mapping images and (d) cross-sectional profile of sample corresponding to Figure 1d'; in EDX mapping images, blue, red, and green colors correspond to Fe, Si, and O, respectively.

4. Formation and Light Emission Properties of Fe-Silicide Core/Si-Shell Quantum Dots

Based on these results, we applied the same processes as discussed for the SOI substrate, as illustrated in Figure 1, to form a new type of superatom structure, namely, Fe-silicide core/Si-shell QD on an ultrathin SiO₂ layer. Figure 3a–f shows the results of the AFM topographic images and the dot height distribution evaluated from each AFM image taken after each process step. Firstly, uniformly sized Si-QDs with an areal density as high as $\sim 10^{11}$ cm⁻² were self-assembled on a ~ 3.0 nm thick SiO₂ layer/p-Si (100) by precisely controlling the low-pressure chemical vapor deposition (LPCVD) using SiH₄ gas, where the average dot height calculated using a log-normal fitting function was estimated to be ~ 5.1 nm. After the ~ 1.0 nm thick Fe film deposition, the surface morphology was slightly smeared, and the average dot height slightly decreased to ~ 3.9 nm. However, after the HCl treatment, the dot height became the same size, which was ~ 5.1 nm as that of the as-grown Si-QDs. This result can be explained by complete removal of the unreacted Fe and Fe oxide by the HCl treatment. Subsequent SiH₄ exposure at 400 °C resulted in a slight increase up to ~ 5.9 nm with no change in the areal dot density. We also confirmed that no Si deposition occurred on the SiO₂ surface at 400 °C because the decomposition temperature of SiH₄ was not reached. Therefore, a slight increase in the average dot height after SiH₄ exposure can be explained by selective growth of Si on top of the dots. Considering the results of the SOI discussed earlier, these results are expected to form β -FeSi₂ core/Si-shell QDs, as schematically illustrated in Figure 3a'–d'. This indicates that the silicidation reaction of the Si-QDs' surface occurred immediately after Fe film deposition. Subsequently, the unreactive Fe films were etched by the HCl treatment. Followed by SiH₄ exposure, Si was selectively grown on the Fe silicide surface, acting as an outer cladding.

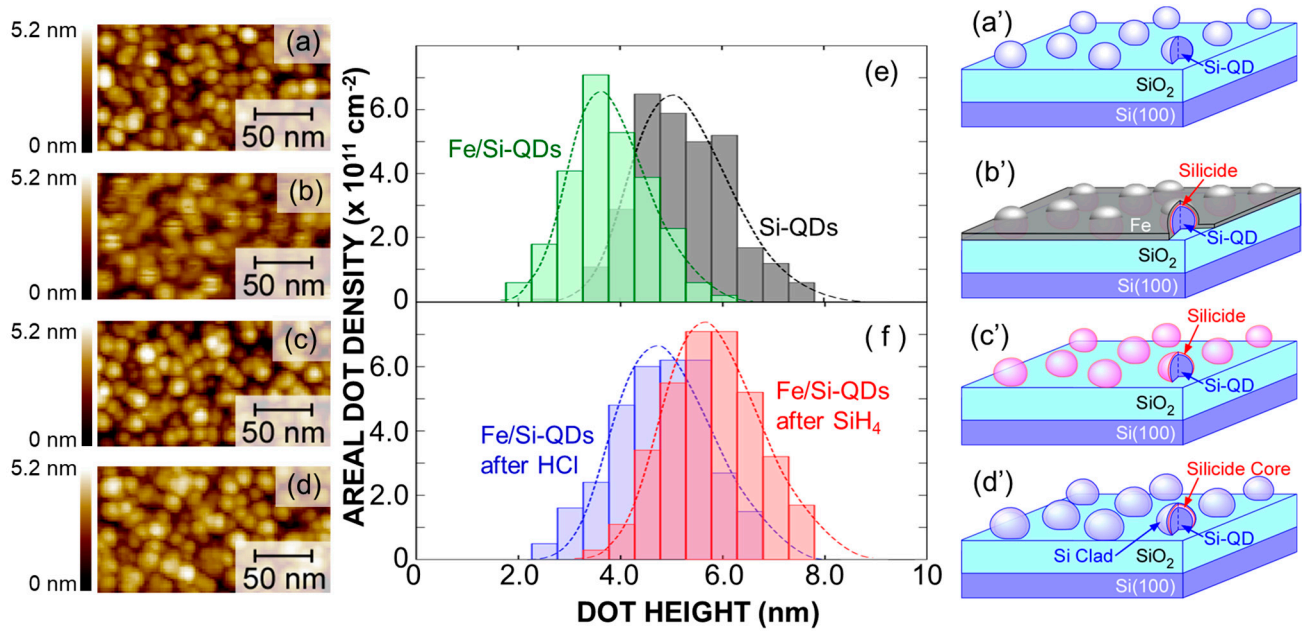


Figure 3. (a–d) Typical AFM images, (e,f) dot height distribution evaluated from AFM images, and (a'–d') schematic illustrations of (a,a') pre-grown Si-QDs, (b,b') after Fe film deposition, (c,c') after HCl treatment, and (d,d') subsequent SiH₄ exposure, wherein dot height distribution and corresponding curves denote log-normal functions well fitted to measured size distribution.

To clarify the crystalline phase of the silicide core, we measured the room temperature PL, using a semiconductor laser with a wavelength of 976 nm at an input power of ~ 0.33 W/cm² as an excitation source and a cooled InGaAs detector, as shown in Figure 4a. Although a weak PL signal in the range from ~ 0.73 to 0.83 eV was observed immediately after the Fe deposition, light emission from the sample was hardly detected after HCl treatment. These results can be explained as follows: immediately after the Fe film deposition, as discussed in Figure 2, β -FeSi₂ layer was formed on the Si-QDs surface despite the oxidation. On the other hand, after HCl treatment, non-radiative recombination centers at the β -FeSi₂ surface dominated due to the complete etching of the surface oxide. It should be noted that, after SiH₄ exposure, light emission with no significant change in wavelength was observed, and the PL intensity drastically increased by a factor of five compared to that after Fe film deposition. This result provides clear evidence for the formation of core/shell dots, indicating that the ultrathin Si cap layer was conformally covered with the dots, resulting in the suppression of defects on the β -FeSi₂ surface. In addition, the PL signal was narrower than that of β -FeSi₂ NDs with an average height of ~ 5 nm formed by SiH₄ exposure of Fe nanodots, as shown in Figure 4b,c. This result can be interpreted in terms of the formation of very uniformly sized core/shell dots compared to the β -FeSi₂ nanodots, as presented in Figure 4e,f, where the full-width and half-maximum value is ~ 2.4 nm for the β -FeSi₂ NDs and ~ 1.9 nm for the core/shell QDs. To analyze the transition processes, the PL spectrum of the β -FeSi₂ core/Si-shell QDs was precisely deconvoluted using four Gaussian curves and compared with that of the β -FeSi₂ NDs, as indicated in Figure 4b,c. As discussed in ref. [48], the PL signal of the β -FeSi₂ NDs can be deconvoluted into three main components, which peaked at ~ 0.79 (Component 1), ~ 0.72 (Component 2), and ~ 0.84 eV (Component 3) in Figure 4b, in which Comp. 1 can be attributed to the radiative recombination of photogenerated electron–hole pairs through discrete quantized states of β -FeSi₂ NDs considering the bandgap of single-crystal β -FeSi₂ bulk. In addition, the radiative transition between the higher-order quantized states in the conduction and valence bands of the β -FeSi₂ NDs is likely responsible for the higher-

energy Comp. 2, as illustrated in Figure 5a. Therefore, Comp. 3 can be attributed to defects in the β -FeSi₂ NDs and/or the interface between the SiO₂ and NDs. In contrast, the PL spectrum of the β -FeSi₂ core/Si-shell QDs was deconvoluted into mainly two components, and the lowest component was hardly detected. However, even though the silicide layer of the core/shell dots is thinner than that of the dots, each PL component is shifted to lower energy compared to the components of the β -FeSi₂ NDs. In semiconductor nanostructures, the PL peak energy shifts toward the higher energy side while decreasing in size due to quantum confinement effects. Therefore, this energy shift cannot be explained by the size effect of the semiconductor nanostructures. To evaluate the influence of core size in such core/shell structures, a systematic investigation involving the fabrication of Si-QD with different sized β -FeSi₂ core, as demonstrated in ref. [31], is required. Nevertheless, considering the energy band diagram of the β -FeSi₂ core/Si-Shell structure, Comp. 1, which has a lower energy emission, might be attributable to radiative recombination between the quantized states in the conduction band of the β -FeSi₂ core and the valence band of the Si shell, as illustrated in Figure 5b, because electrons are confined in the conduction band of the β -FeSi₂ core, and holes can be confined in the shallow potential well of the valence band of the Si clad and penetrate the β -FeSi₂ core for radiative recombination in this system.

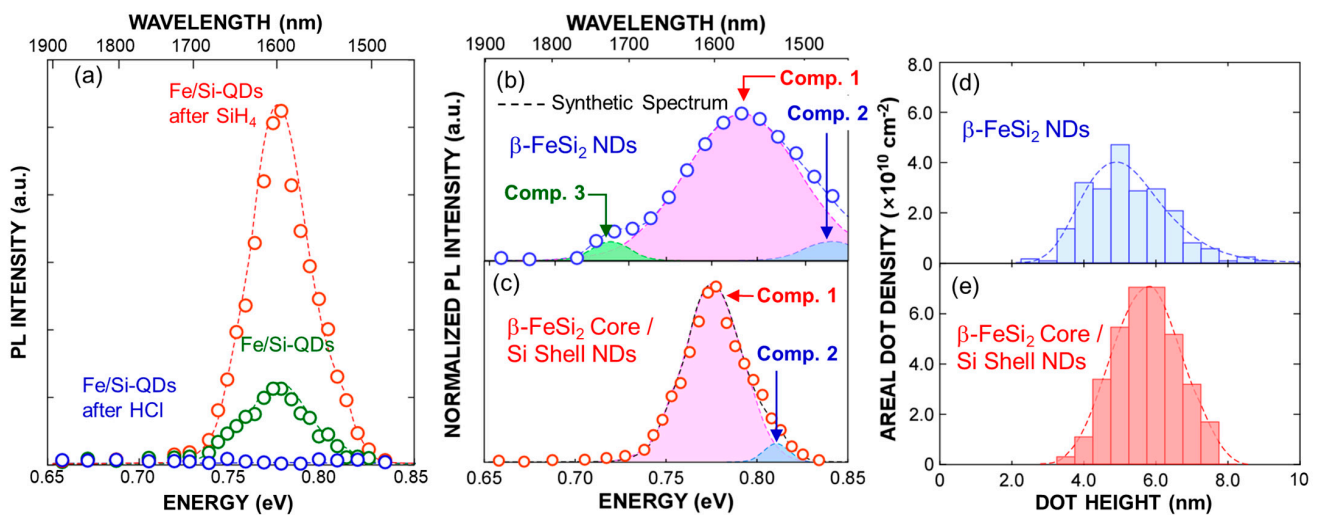


Figure 4. (a–c) Room temperature PL spectra of (a,c) NDs are illustrated in Figure 3, and (b) β -FeSi₂-NDs taken under 967 nm light excitations, and (b,c) their deconvoluted spectra evaluated from spectral analysis using Gaussian curve fitting method, where synthetic spectrum of deconvoluted spectra is also shown as dashed line. Dot height distribution of (d) β -FeSi₂ NDs and (e) β -FeSi₂ core/Si-shell QDs.

The results obtained in this work show that the β -FeSi₂ core/Si-shell QDs have narrow PL spectra in the region of 0.74–0.84 eV at room temperature, suggesting that the radiative recombination of photo-generated carriers through quantized states of the core is the dominant pathway for the emission from the dots, reflecting the energy band discontinuity between the Si clad and FeSi₂ core. This means that the β -FeSi₂ core/Si-shell QDs can be regarded as active elements in optical applications with very few defects at the interface and/or surface, making them one of the most technologically important materials. Furthermore, our samples are highly compatible with the Si-ULSI processing technology. We believe that our findings will pave the way for constructing Si-based photonic processing that exhibits high thermal stability, low power consumption, and room temperature operation.

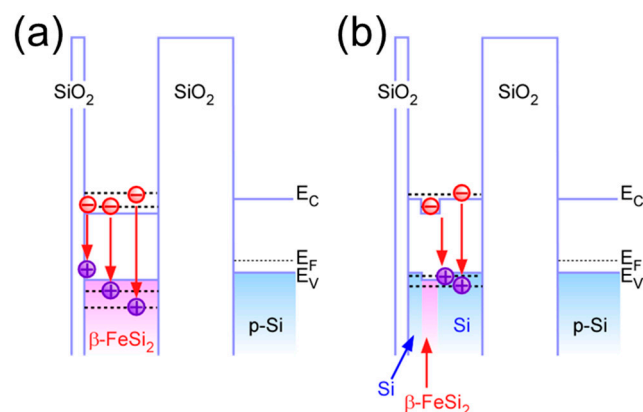


Figure 5. Energy band diagram of (a) β -FeSi₂-NDs and (b) β -FeSi₂ core/Si-shell QDs, illustrating radiative transition corresponding to PL components as shown in Figure 4b,c.

5. Conclusions

We fabricated highly dense β -FeSi₂ core/Si-shell QDs with an areal density as high as $\sim 10^{11}$ cm⁻² on an ultrathin SiO₂ layer and evaluated their room temperature light emission properties. We confirmed a clear light emission in the near-infrared region at room temperature. The origin of this light emission under weak excitation is considered to be the radiative recombination between the quantized states in the conduction band of the β -FeSi₂ core and the valence band of the Si shell. Although the β -FeSi₂ core/Si shell QDs fabricated in this study are extremely small in size, their areal density likely results in limited absorption of incident light, leading to low quantum efficiency. Nonetheless, the light emission intensity could be significantly improved by increasing the dot density or by implementing multilayer stacking structures. From a technological point of view, it is quite important that such narrow light emission in the spectral width at room temperature could be achieved using the β -FeSi₂ core/Si-shell QDs, which have very few defects at the interface between the QD and its surface. The results lead to the development of Si-based light-emitting devices that are highly compatible with Si-ULSI processing, which was found difficult to realize in silicon photonics.

Author Contributions: Conceptualization, K.M.; methodology, K.M.; formal analysis, K.M.; investigation, Y.Y. and M.A.S.; writing—original draft preparation, K.M.; project administration, A.M. and S.M. All authors have read and agreed to the published version of the manuscript.

Funding: This work was supported in part by the Grant-in-Aid for Scientific Research (A) 21H04559, the Fund for the Promotion of Joint Intentional Research [Fostering Joint International Research (A)] 18KK0409 of MEXT Japan, and Hibi Science Foundation.

Data Availability Statement: The original contributions presented in this study are included in the article. Further inquiries can be directed to the corresponding author.

Acknowledgments: The authors thank the IHP cleanroom staff epitaxy process team for their excellent support.

Conflicts of Interest: The authors declare no conflicts of interest.

References

1. Soref, R.A.; Lorenzo, J.P. Single-crystal silicon: A new material for 1.3 and 1.6 μ m integrated-optical components. *Electron. Lett.* **1985**, *21*, 953–954. [[CrossRef](#)]
2. Schmidtchen, J.; Splett, A.; Schüppert, B.; Petermann, K.; Burbach, G. Low loss singlemode optical waveguides with large cross-section in silicon-on-insulator. *Electron. Lett.* **1991**, *27*, 1486–1488. [[CrossRef](#)]

3. Weiss, B.L.; Reed, G.T.; Toh, S.K.; Soref, R.A.; Namavar, F. Optical waveguides in SIMOX structures. *IEEE Photonics Technol. Lett.* **1991**, *3*, 19–21. [[CrossRef](#)] [[PubMed](#)]
4. Liu, A.; Jones, R.; Liao, L.; Samara-Rubio, D.; Rubin, D.; Cohen, O.; Nicolaescu, R.; Paniccia, M. A high-speed silicon optical modulator based on a metal–oxide–semiconductor capacitor. *Nature* **2004**, *427*, 615–618. [[CrossRef](#)]
5. Liao, L.; Samara-Rubio, D.; Morse, M.; Liu, A.; Hodge, D.; Rubin, D.; Keil, U.D.; Franck, T. High speed silicon mach-zehnder modulator. *Opt. Express* **2005**, *13*, 3129–3135. [[CrossRef](#)]
6. Liao, L.; Liu, A.; Rubin, D.; Basak, J.; Chetrit, Y.; Nguyen, H.; Cohen, R.; Izhaky, N.; Paniccia, M. 40 Gbit/s silicon optical modulator for high-speed applications. *Electron. Lett.* **2007**, *43*, 1196–1197. [[CrossRef](#)]
7. Dehlinger, G.; Koester, S.J.; Schaub, J.D.; Chu, J.O.; Ouyang, Q.C.; Grill, A. High-speed Germanium-on-SOI lateral PIN photodiodes. *IEEE Photonics Technol. Lett.* **2004**, *16*, 2547–2549. [[CrossRef](#)]
8. Ahn, D.; Hong, C.-Y.; Liu, J.; Giziewicz, W.; Beals, M.; Kimerling, L.C.; Michel, J.; Chen, J.; Kärtner, F.X. High performance, waveguide integrated Ge photodetectors. *Opt. Express* **2007**, *15*, 3916–3921. [[CrossRef](#)]
9. Shekhar, S.; Bogaerts, W.; Chrostowski, L.; Bowers, J.E.; Hochberg, M.; Soref, R.; Shastri, B.J. Roadmapping the next generation of silicon photonics. *Nat. Commun.* **2024**, *10*, 751. [[CrossRef](#)]
10. Zakharov, N.D.; Talalaev, V.G.; Werner, P.; Tonkikh, A.A.; Cirlin, G.E. Room-temperature light emission from a highly strained Si/Ge superlattice. *Appl. Phys. Lett.* **2003**, *83*, 3084–3086. [[CrossRef](#)]
11. Jambois, O.; Rinnert, H.; Devaux, X.; Vergnat, M. Photoluminescence and electroluminescence of size-controlled silicon nanocrystallites embedded in SiO₂ thin films. *J. Appl. Phys.* **2005**, *98*, 046105. [[CrossRef](#)]
12. Sun, K.W.; Sue, S.H.; Liu, C.W. Visible photoluminescence from Ge quantum dots. *Phys. E Low-Dimens. Syst. Nanostruct.* **2005**, *28*, 525–530. [[CrossRef](#)]
13. del Pino, A.P.; Gyorgy, E.; Marcus, I.C.; Roqueta, J.; Alonso, M.I. Effects of pulsed laser radiation on epitaxial self-assembled Ge quantum dots grown on Si substrates. *Nanotechnology* **2011**, *22*, 295304. [[CrossRef](#)] [[PubMed](#)]
14. Gassenq, A.; Guillois, K.; Pauc, N.; Hartmann, J.-M.; Dias, G.O.; Rouchon, D.; Tardif, S.; Escalante, J.; Duchemin, I.; Niquet, Y.-M.; et al. Study of the light emission in Ge layers and strained membranes on Si substrates. *Thin Solid Films* **2016**, *613*, 64–67. [[CrossRef](#)]
15. Schlykowsky, V.; Zaumseil, P.; Schubert, M.A.; Skibitzki, O.; Yamamoto, Y.; Klesse, W.M.; Hou, Y.; Virgilio, M.; De Seta, M.; Di Gaspare, L.; et al. Photoluminescence from GeSn nano-heterostructures. *Nanotechnology* **2018**, *29*, 415702. [[CrossRef](#)]
16. Thai, Q.M.; Pauc, N.; Aubin, J.; Bertrand, M.; Chrétien, J.; Delaye, V.; Chelnokov, A.; Hartmann, J.-M.; Reboud, V.; Calvo, V. GeSn heterostructure micro-disk laser operating at 230 K. *Opt. Express* **2018**, *26*, 32500–32508. [[CrossRef](#)]
17. Von den Driesch, N.; Stange, D.; Rainko, D.; Breuer, U.; Capellini, G.; Hartmann, J.-M.; Sigg, H.; Mantl, S.; Grützmacher, D.; Buca, D. Epitaxy of Si-Ge-Sn-based heterostructures for CMOS-integratable light emitters. *Solid-State Electron.* **2019**, *155*, 139–143. [[CrossRef](#)]
18. Chrétien, J.; Pauc, N.; Pilon, F.A.; Bertrand, M.; Thai, Q.-M.; Casiez, L.; Bernier, N.; Dansas, H.; Gergaud, P.; Delamadeleine, E.; et al. GeSn Lasers Covering a Wide Wavelength Range Thanks to Uniaxial Tensile Strain. *ACS Photonics* **2019**, *6*, 2462–2469. [[CrossRef](#)]
19. Armand Pilon, F.T.; Lyasota, A.; Niquet, Y.-M.; Reboud, V.; Calvo, V.; Pauc, N.; Widiez, J.; Bonzon, C.; Hartmann, J.-M.; Chelnokov, A.; et al. Lasing in strained germanium microbridges. *Nat. Commun.* **2019**, *10*, 2724. [[CrossRef](#)]
20. Fadaly, E.M.T.; Dijkstra, A.; Suckert, J.R.; Ziss, D.; van Tilburg, M.A.J.; Mao, C.; Ren, Y.; van Lange, V.T.; Korzun, K.; Kölling, S.; et al. Direct bandgap emission from hexagonal Ge and SiGe alloys. *Nature* **2020**, *580*, 205–209. [[CrossRef](#)]
21. Ji, Z.-M.; Luo, J.-W.; Li, S.-S. Interface-engineering enhanced light emission from Si/Ge quantum dots. *New J. Phys.* **2020**, *22*, 093037. [[CrossRef](#)]
22. Jannesari, R.; Schatzl, M.; Hackl, F.; Glaser, M.; Hingerl, K.; Fromherz, T.; Schäffler, F. Commensurate germanium light emitters in silicon-on-insulator photonic crystal slabs. *Opt. Express* **2014**, *22*, 25426–25435. [[CrossRef](#)] [[PubMed](#)]
23. Petykiewicz, J.; Nam, D.; Sukhdeo, D.S.; Gupta, S.; Buckley, S.; Piggott, A.Y.; Vučković, J.; Saraswat, K.C. Direct Bandgap Light Emission from Strained Germanium Nanowires Coupled with High-Q Nanophotonic Cavities. *Nano Lett.* **2016**, *16*, 2168–2173. [[CrossRef](#)] [[PubMed](#)]
24. Reboud, V.; Gassenq, A.; Hartmann, J.M.; Widiez, J.; Virost, L.; Aubin, J.; Guillois, K.; Tardif, S.; Fédéli, J.M.; Pauc, N.; et al. Germanium based photonic components toward a full silicon/germanium photonic platform. *Prog. Cryst. Growth Charact. Mater.* **2017**, *63*, 1–24. [[CrossRef](#)]
25. Walters, R.J.; Bourianoff, G.I.; Atwater, H.A. Field-effect electroluminescence in silicon nanocrystals. *Nat. Mater.* **2005**, *4*, 143–146. [[CrossRef](#)]
26. Xu, X.; Tsuboi, T.; Chiba, T.; Usami, N.; Maruizumi, T.; Shiraki, Y. Silicon-based current-injected light emitting diodes with Ge self-assembled quantum dots embedded in photonic crystal nanocavities. *Opt. Express* **2012**, *20*, 14714–14721. [[CrossRef](#)]
27. Xu, X.; Usami, N.; Maruizumi, T.; Shiraki, Y. Enhancement of light emission from Ge quantum dots by photonic crystal nanocavities at room-temperature. *J. Cryst. Growth* **2013**, *378*, 636. [[CrossRef](#)]

28. Xu, X.; Maruizumi, T.; Shiraki, Y. Waveguide-integrated microdisk light-emitting diode and photodetector based on Ge quantum dots. *Opt. Express* **2014**, *22*, 3902–3910. [[CrossRef](#)]
29. Zeng, C.; Ma, Y.; Zhang, Y.; Li, D.; Huang, Z.; Wang, Y.; Huang, Q.; Li, J.; Zhong, Z.; Yu, J.; et al. Single germanium quantum dot embedded in photonic crystal nanocavity for light emitter on silicon chip. *Opt. Express* **2015**, *23*, 22250–22261. [[CrossRef](#)]
30. Makihara, K.; Kondo, K.; Ikeda, M.; Ohta, A.; Miyazaki, S. Photoluminescence Study of Si Quantum Dots with Ge Core. *ECS Trans.* **2014**, *64*, 365–370. [[CrossRef](#)]
31. Yamada, K.; Kondo, K.; Makihara, K.; Ikeda, M.; Ohta, A.; Miyazaki, S. Effect of Ge Core Size on Photoluminescence from Si Quantum Dots with Ge Core. *ECS Trans.* **2016**, *75*, 695–700. [[CrossRef](#)]
32. Kondo, K.; Makihara, K.; Ikeda, M.; Miyazaki, S. Photoluminescence study of high density Si quantum dots with Ge core. *J. Appl. Phys.* **2016**, *119*, 033103. [[CrossRef](#)]
33. Makihara, K.; Ikeda, M.; Fujimura, N.; Yamada, K.; Ohta, A.; Miyazaki, S. Electroluminescence of superatom-like Ge-core/Si-shell quantum dots by alternate field-effect-induced carrier injection. *Appl. Phys. Express* **2018**, *11*, 011305. [[CrossRef](#)]
34. Makihara, K.; Yamamoto, Y.; Imai, Y.; Taoka, N.; Schubert, M.A.; Tillack, B.; Miyazaki, S. Room Temperature Light Emission from Superatom-like Ge-core/Si-shell Quantum Dots. *Nanomaterials* **2023**, *13*, 1475. [[CrossRef](#)]
35. Bost, M.C.; Mahan, J.E. Optical properties of semiconducting iron disilicide thin films. *J. Appl. Phys.* **1985**, *58*, 2696–2703. [[CrossRef](#)]
36. Katsumata, H.; Makita, Y.; Kobayashi, N.; Shibata, H.; Hasegawa, M.; Aksenov, I.; Kimura, S.; Obara, A.; Uekusa, S.-I. Optical absorption and photoluminescence studies of β -FeSi₂ prepared by heavy implantation of Fe⁺ ions into Si. *J. Appl. Phys.* **1996**, *80*, 5955–5962. [[CrossRef](#)]
37. Leong, D.; Harry, M.; Reeson, K.J.; Homewood, K.P. A silicon/iron-disilicide light-emitting diode operating at a wavelength of 1.5 μ m. *Nature* **1997**, *387*, 686–688. [[CrossRef](#)]
38. Suemasu, T.; Negishi, Y.; Takakura, K.; Hasegawa, F.; Chikyow, T. Influence of Si growth temperature for embedding β -FeSi₂ and resultant strain in β -FeSi₂ on light emission from p-Si/ β -FeSi₂ particles/n-Si light-emitting diodes. *Appl. Phys. Lett.* **2001**, *79*, 1804–1806. [[CrossRef](#)]
39. Nakamura, T.; Tatsumi, T.; Morita, K.; Kobayashi, H.; Noguchi, Y.; Kawakubo, Y.; Maeda, Y. Photoluminescence Property of Nano-Composite Phases of β -FeSi₂ Nanocrystals Embedded in SiO₂. *JJAP Conf. Proc.* **2015**, *3*, 011106. [[CrossRef](#)]
40. Lourenco, M.A.; Butler, T.M.; Kewell, A.K.; Gwilliam, R.M.; Kirkby, K.J.; Homewood, K.P. Electroluminescence of β -FeSi₂ Light Emitting Devices. *Jpn. J. Appl. Phys.* **2001**, *40*, 4041–4044. [[CrossRef](#)]
41. Martinelli, L.; Grilli, E.; Guzzi, M.; Grimaldi, M.G. Room-temperature electroluminescence of ion-beam-synthesized β -FeSi₂ precipitates in silicon. *Appl. Phys. Lett.* **2003**, *83*, 794. [[CrossRef](#)]
42. Li, C.; Ozawa, Y.; Suemasu, T.; Hasegawa, F. Thermal Enhancement of 1.6 μ m Electroluminescence from a Si-Based Light-Emitting Diode with β -FeSi₂ Active Region. *Jpn. J. Appl. Phys.* **2004**, *43*, L1492.
43. Sunohara, T.; Kobayashi, K.; Suemasu, T. Epitaxial growth and characterization of Si-based light-emitting Si/ β -FeSi₂ film/Si double heterostructures on Si(001) substrates by molecular beam epitaxy. *Thin Solid Films* **2006**, *508*, 371–375. [[CrossRef](#)]
44. Miyazaki, S.; Hamamoto, Y.; Yoshida, E.; Ikeda, M.; Hirose, M. Control of Self-Assembling Formation of Nanometer Silicon Dots by Low Pressure Chemical Vapor Deposition. *Thin Solid Films* **2000**, *369*, 55–59. [[CrossRef](#)]
45. Takami, H.; Makihara, K.; Ikeda, M.; Miyazaki, S. Characterization of Electroluminescence from One-dimensionally Self-Aligned Si-based Quantum Dots. *Jpn. J. Appl. Phys.* **2013**, *52*, 04CG08. [[CrossRef](#)]
46. Yamada, T.; Makihara, K.; Ohta, A.; Ikeda, M.; Miyazaki, S. Study on electroluminescence from multiply-stacking valency controlled Si quantum dots. *Thin Solid Films* **2016**, *602*, 48–51. [[CrossRef](#)]
47. Furuhashi, H.; Makihara, K.; Shimura, Y.; Fujimori, S.; Imai, Y.; Ohta, A.; Taoka, N.; Miyazaki, S. Study on Silicidation Reaction of Fe-NDs with SiH₄. *Appl. Phys. Express* **2022**, *15*, 055503. [[CrossRef](#)]
48. Miyazaki, S.; Makihara, K. Formation and Characterization of Fe-Silicide Nanodots for Optoelectronic Application. *ECS Trans.* **2023**, *112*, 131–137. [[CrossRef](#)]
49. Saito, H.; Makihara, K.; Taoka, N.; Miyazaki, S. Formation of β -FeSi₂ NDs by SiH₄-exposure to Fe-NDs. *Jpn. J. Appl. Phys.* **2024**, *63*, 02SP99. [[CrossRef](#)]
50. Canali, C.; Majni, G.; Ottaviani, G.; Celotti, G. Phase diagrams and metal-rich silicide formation. *J. Appl. Phys.* **1979**, *50*, 255–258. [[CrossRef](#)]
51. Ikarashi, N.; Masuzaki, K. Silicide formation process in ultra-thin Ni-silicide film for advanced semiconductor devices: Mechanism of NiSi₂ formation at low temperature. *J. Phys. Conf. Ser.* **2011**, *326*, 012051. [[CrossRef](#)]

Disclaimer/Publisher’s Note: The statements, opinions and data contained in all publications are solely those of the individual author(s) and contributor(s) and not of MDPI and/or the editor(s). MDPI and/or the editor(s) disclaim responsibility for any injury to people or property resulting from any ideas, methods, instructions or products referred to in the content.